



Structural, FTIR, optical and dielectric properties of $\text{Zn}_{1-x}\text{Al}_x\text{O}$ ceramics for advanced applications

A. Sedky¹ · Atif Mossad Ali² · H. Algarni²

Received: 28 December 2021 / Accepted: 22 April 2022 / Published online: 25 May 2022

© The Author(s), under exclusive licence to Springer Science+Business Media, LLC, part of Springer Nature 2022, corrected publication 2022

Abstract

We report here the structural, FTIR, optical and dielectric properties of $\text{Zn}_{1-x}\text{Al}_x\text{O}$ with $x = 0.00 \leq x \leq 0.20$). The samples are synthesized by the solid state reaction method and the phase purity, structural morphology, and absorption spectra are examined by XRD, SEM, and FTIR techniques. The optical and dielectric measurements are obtained by a double beam spectrophotometer and an impedance analyzer. The wurtzite structure is confirmed for all samples, and the lattice parameters, crystallite diameter, and porosity are decreased by Al, whereas the Debye temperature and elastic modulus are increased. The residual stress is compressive for ZnO, but it is changed to tensile for the doped samples. Two different values of energy gap (E_{gh} and E_{gl}) are apparent for each sample. The E_{gh} and E_{gl} are, respectively, 3.60, 3.56, 3.43, 3.53, 3.68 eV and 3.02, 2.95, 2.85, 2.92, 3.07 eV for all samples such that $\Delta E = (E_{\text{gh}} - E_{\text{gl}}) \sim 0.60$. The residual dielectric lattice constant is decreased by increasing x to 0.10, followed by a sharp increase at $x = 0.20$, while the opposite behavior is obtained for (N/m^*) . The dielectric constant and ac conductivity are slightly increased as x increases to 0.025, followed by a sharp increase with more increase of x to 0.20. The conduction is electronic for pure and $x = 0.025$ samples, but it changes to hole with increasing x to 0.20. The binding energy was decreased as x increased to 0.20, but there is no exact trend for the hopping distance and density of localized states against x . The F-factor for solar cell design was increased as x increased to 0.10, but it is almost constant at $x = 0.20$. The Cole–Cole plot is a straight line for $x = 0.00$, a semicircle arc for $x = 0.025$, and a complete semicircle for $x \geq 0.05$. The impedance resistance of grain and grain boundaries decreases as x increases to 0.20. These outcomes indicate that the addition of Al to ZnO shifts the mechanical, optical, and dielectric medium to higher values, which is strongly recommended for the design of optoelectronic and solar cell instruments.

Keywords Al doped ZnO · Elastic modulus · Energy gap · Dielectric medium and · F-factor

✉ A. Sedky
sedky196000@hotmail.com; sedky1@aun.edu.eg

¹ Department of Physics, Faculty of Science, Assiut University, Assiut 71516, Egypt

² Physics Department, Faculty of Science, King Khalid University, Abha, Saudi Arabia

1 Introduction

Wurtzite structure of pure n-type ZnO with 3.2 eV band gap (E_g) and 60 Urbach energy has been used in varistors, optoelectronic and solar cell devices (Manikandan et al. 2017; Ragupathi et al. 2013; Kumar et al. 2015). ZnO has been synthesised by the solid state reaction method through sintering at high temperatures followed by quenching in air to RT (Mohamed and Abu-Dief 2018; Mustaqima 2014; Djerdj and Jaglicić et al., 2019; Yang 2013). However, the properties of ZnO are controlled by intrinsic defects such as oxygen vacancies generated during sintering and also be improved by quenching (Amin and Sedky 2019; Sedky et al. 2007). Despite the existence of advantageous chemical techniques for ZnO synthesis, the solid-state method is still of interest because it governs the ZnO to work as a varistor (Mohamed and Abu-Dief 2020). However, oxygen vacancies in ZnO can exist in three charge states, i.e., V_o^0 , V_o^+ , and V_o^{++} , respectively. The V_o^0 and V_o^{++} charged are stable, while V_o^+ is unstable and it is usually changed into V_o^{++} by capturing electrons from the CB. However, due to V_o^{++} defects (10^{19} cm^{-3}), some of the energy states lie at about 0.86 eV above the valence band (VB), which can affect the E_g of ZnO to be qualified for practical applications (Vempati et al. 2012; Rodnyi et al. 2018a).

The mechanism of the ZnO conduction band (CB) usually arises when the 4 s orbital of Zn is wide enough to allow for effective charge transfer (Mohamed et al. 2022; Kumar and Rani 2013; Abdullah et al. 2012). Consequently, the electrons are excited from the VB due to the absorption of light, and consequently the electron–hole pairs are generated. Above the limit of the E_g , the recorded signals of photon energy are due to non-radiative and Urbach tail processes. However, the energy of photons for creating electron–hole pairs (e–h) can be considered only for materials with a larger Urbach energy like ZnO (Sedky et al. 2020). In order to improve the optical properties, ZnO has 3-d transition metals (Shahedi and Jafari 2017; Raghu et al. 2017). Among these elements, Al doped ZnO is considered as an alternative for solar cells and light-emitting diodes (LEDs) as a result of the extra free electron formed in the ZnO CB (Wang and Zhang 2017; Zhai et al. 2016; Al-Naim et al. 2021). It is also approved that Al decreased the particle size and slightly increased the E_g of ZnO, which is attributed to the Al impurity incorporation or structural defects (Al-Naim et al. 2021; Diqiu et al. 2013; Kamarulzama 2015). Due to the extrinsic Al dopant, the CB of ZnO can be partially filled with free electrons of Al^{3+} , resulting in an E_g increase. However, when the carrier concentration exceeds $5 \times 10^{20} \text{ cm}^{-3}$, E_g shrinkage may occur due to carrier renormalization of carriers (Tong et al. 2011; Li et al. 2014a). In addition, Al can also affect the excitonic absorption near the band edge due to the free-electron screening effect (Li et al. 2014b). Therefore, it is interesting to examine the influence of Al on the optical constants of ZnO.

The electronic traps of ZnO are mainly localized at the grain boundaries and usually adsorbed with oxygen. They also capture some donor state electrons (Deng 2016). Consequently, the Schottky barrier capacitance is found to be frequency dependent due to the finite time constants τ ($\tau = (1/\omega) = RC$) of the deep trap states generated in the depletion layer (Arda et al. 2013). Ac impedance spectroscopy is able to separate the electric response in different regions of ZnO within the range of τ (Ram et al. 2016). This response is entirely characterized by the complex dielectric parameters that govern ac field frequency response (Sedky et al. 2022a).

Materials with high dielectric constants such as ZnO have received special attention due to the rapid developments in telecommunications and multilayer capacitors are required for microwave integrated circuits (Tripathi et al. 2010, Saadi et al. 2020, Sajid Ali et al.

2012). In contrast, materials that have a low dielectric constant are potential candidates for nonlinear optical and high-frequency devices, which are necessary for such applications (Saadi et al. 2020). However, some parameters have a great influence on improving ZnO dielectric constants, such as valence state, content, magnetic moment of TM, and also intrinsic defects (Sajid Ali et al. 2012; Singh et al. 2015; Zamiri et al. 2013; Irshad et al. 2018). However, the dielectric properties of ZnO can be tuned by introducing dopants into the ZnO host matrix such as 3-d transition-elements (TM) (Omri et al. 2018; Joshi et al. 2014; Singh and Singh 2020a; Das et al. 2017). For example, a significant enhancement in dielectric constant resulted from the incorporation of Al in the ZnO lattice, while an opposite trend was observed for dielectric loss. In addition, the ac electrical conductivity of Al-doped ZnO samples increased due to the availability of charge carriers and defects by Al (Saadi et al. 2020; ChediaBelkhaoui 2019; Sedky et al. 2019; Kant and Sharma 2021).

The electrical properties of Al doped with ZnO are presented by Sedky et al. (2019; Khan and Fashu 2017). It is found the addition of Al generally decreases the nonlinear behavior of ZnO and, therefore, the DC electrical conductivity has increased. It is believed that the excess electron density and structural distortion, produced by Al doping in both under and over doped regions, are responsible for the above behavior. With this purpose in mind, structural, FTIR analysis, optical and dielectric behaviors will be examined on the same batch of samples. For such applications, some important physical parameters, such as Debye temperatures, elastic constants, energy gap, dielectric loss, N/m^3 , inter-atomic distance R , density of states at Fermi level $N(E_F)$, F-factor, and ac impedance, are well estimated. These outcomes indicate that AlZnO samples are strongly recommended for the design of optoelectronic and solar cell instruments.

2 Experimental details

$Zn_{1-x}Al_xO$ samples with $x = 0.00, 0.05, 0.10, 0.20$ were synthesised by using the solid-state reaction method. The powders of ZnO and Al_2O_3 (Aldrich 99.999 purity) are thoroughly mixed in the required proportions and calcined at $900^\circ C$ in air for a period of 16 h. The resulting powders are ground, mixed, and pressed into discs (1 cm in diameter and 0.3 cm in thickness). The pellets are then separately sintered at temperature of $1200^\circ C$ for 12 h in the air and then suddenly cooled (quenched) in air to room temperature. The bulk density of the samples is measured in terms of their weight and volume. The phase purity of the samples was tested by XRD using $Cu-K\alpha$ radiation of wave length 1.5418 \AA at 40 kV and 30 mA settings, and $(20^\circ-70^\circ)$ diffraction angles with a step of 0.06° . The structural morphology of the samples is obtained in powder form by scanning electron microscope (SEM) JSM 5400 LV with $2 \mu m$ bar length and 7500 amplification. FTIR absorption spectra of the samples were carried out in the range of $(400-4000 \text{ cm}^{-1})$, with 4 cm^{-1} resolution and 2 (cm/s) scanning speed using a spectrum 400-FT-1R/FT-NIR spectrometer. The samples were homogenized in a spectroscopic grade of KBr carrier in an agate mortar and pressed into 2 mm pellets. The optical properties at room temperature were measured against wavelength (200–1000 nm) using a JascoV-570 (Japan) computer programmable double beam with UV–visible–NIR spectrophotometer at standard incidence with a scan speed of 1000 mm min^{-1} . The complex dielectric measurements were obtained at room temperature using a precision impedance analyzer model 4295A in the frequency range of 1 to 10^7 Hz and 1 V Ac amplitude. The pellets are sandwiched between two gold-plated

stainless steel electrodes of 20 mm in diameter in parallel plate geometry. The ac conductivity and modulus of complex impedance Z as a function of frequency are well recorded. From the impedance spectra, values of the real Z' and the imaginary Z'' parts of the complex impedance could be obtained.

3 Results and discussion

3.1 Structural analysis

It is evident from the XRD patterns shown in Fig. 1a that all samples show a wurtzite structure ICSD 01–079-0208 (space group P63mc) of ZnO. No additional lines could be formed for the samples of $x=0.00$ and 0.025 , but as x is increased to and above 0.025 , some unidentified lower peaks could be seen at $2\theta=30.96^\circ$ for $x=0.05$; $2\theta=30.96^\circ$, 55.5° , 60° for $x=0.10$; and $2\theta=30.96^\circ$, 48.74° , 55.5° , 60° for $x=0.20$. This is because the bond energy of Al_2O_3 is higher than ZnO, and therefore more energy is required for Al ions to enter the ZnO lattice to form the Al-O bond, and therefore some of secondary phases could be formed (Sajid Ali et al. 2012; Khan et al. 2013). The lattice parameters a and c , listed in Table 1, are gradually decreased by increasing x . The c/a , U -parameter and ZnO bond length L are almost the same as reported for ZnO (Mansour Mohamed 2021; Morais et al. 2018). This is due to the smaller ionic size of Al^{3+} (0.51 \AA) than that of Zn^{2+} (0.74 \AA) at the same tetrahedral fold-coordination (Samanta and Goswami 2018; Sedky 2020). As x increases to 0.10 , the porosity calculated by; $PS = [1 - (\rho_{\text{exp}}/\rho_{\text{th}})]$ decreases slightly, followed by an increase at $x=0.20$. This behavior indicated that Al up to 0.10 helps as much as possible for decreasing the number of porous ZnO. However, porosity is the quality of ZnO of being porous, and it is usually evaluated by the ratio of the volume of interstices of ZnO to the volume of its mass. Therefore, Al up to 0.10 can enter the ZnO lattice and thus decreased the volume of interstices, which in turn decreased the porosity. However, at $x=0.20$, some of the Al ions are unable to localize in the ZnO lattice due to the solubility limit, so the porosity was increased, in consistent with XRD analysis.

The crystallite size D_{hkl} given by $D_{\text{hkl}} = \frac{K\lambda}{\beta \cos \theta}$ (Seetawan et al. 1302) for the most intense peaks listed in Table 1 are decreased by x to 0.20 . The vice is versa for dislocation density δ calculated by $(1/D_{\text{hkl}})^2$. The micro-lattice strain $\epsilon_{\text{ms}} = \frac{\beta \cos \theta}{4}$ listed in Table 1 is positive and increased by Al. While lattice strain $\epsilon_{\text{ls}} = (c - c_0)/c_0$ is positive for pure ZnO, but it changes to negative for the doped samples. Regardless of its sign, this behavior indicates that Al helps as a possible ZnO for few lattice defects or distortions. (Wojnarowicz et al. 2018; Aljaafari and Sedky 2020). The SEM micrographs shown in Fig. 1b indicates that nearly, no second phases are formed at grain boundaries, but the grains are randomly distributed over the matrix structure. For simplicity, the average size of the grain (D_{SEM}) is determined by the linear intercept method with the help of expression, $D_{\text{SEM}} = \frac{1.56L}{MN}$ (Wang and Zhang 2017), where L is the length of a random line on the micrograph, M is micrograph magnification, and N is the grain boundary number that is intercepted by the lines. As listed in Table 1, Al content up to $x < 0.10$ decreased the average grain size of ZnO D_{SEM} , followed by an increase at $x=0.20$, which is consistent with D_{hkl} behavior obtained from XRD analysis.

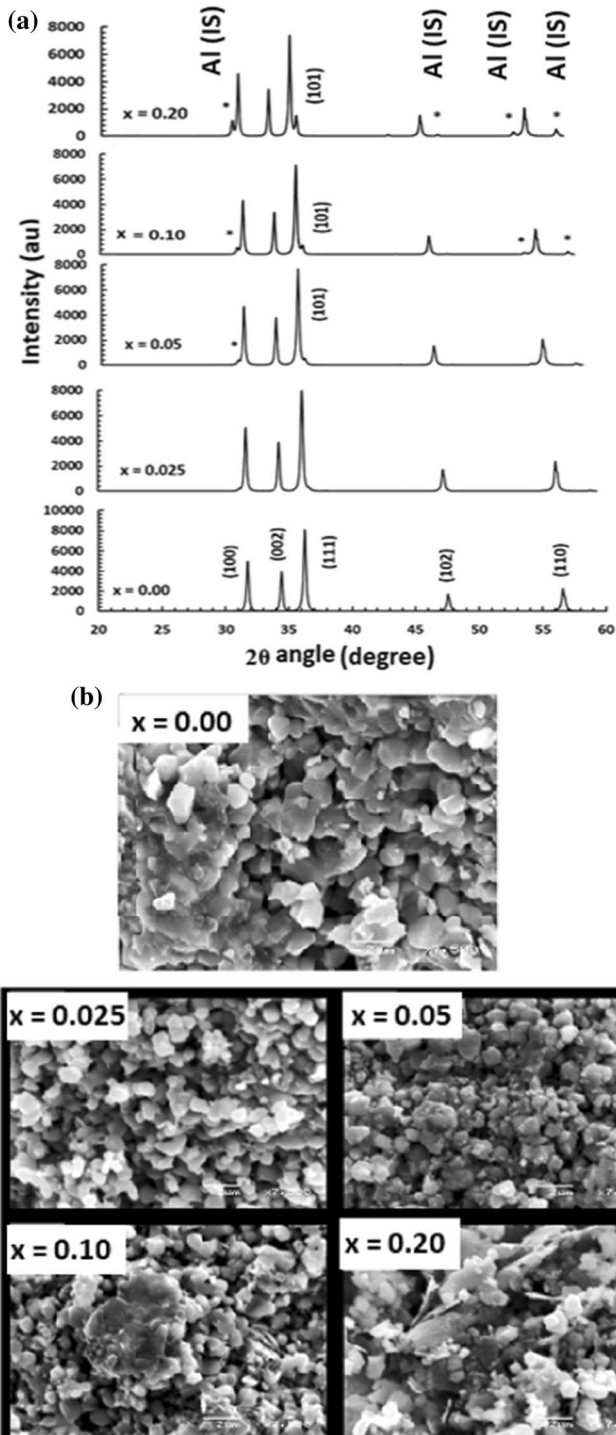


Fig. 1 a XRD patterns for pure and Al doped ZnO samples b SEM micrographs for pure and Al doped ZnO samples

Table 1 I_{avg} , a, c, c/a, V, U, L, δ , ρ , P_s , ϵ_{ms} , ϵ_{ls} , D_{XRD} and D_{SEM} of pure and Al doped ZnO samples

x	a (Å)	c (Å)	c/a	V (Å) ³	$\epsilon_{ls} \times 10^{-3}$	U	L (Å)
0.00	3.252	5.208	1.601	47.697	0.27	0.379	1.991
0.025	3.247	5.201	1.602	47.486	– .08	0.380	1.987
0.05	3.242	5.196	1.603	47.295	–2.04	0.380	1.987
0.10	3.231	5.188	1.606	46.902	–3.57	0.380	1.990
0.20	3.237	5.191	1.604	46.665	–4.92	0.380	1.981
x	ρ_{th} (g/cm ³)	ρ_{exp} (g/cm ³)	P_s	D_{XRD} (nm)	$\delta \times 10^{-4}(\text{nm})^{-2}$	$\epsilon_{ms} \times 10^{-3}$	D_{SEM} (μm)
0.00	5.794	5.451	0.059	41.830	5.72	3.32	2.060
0.025	5.630	5.312	0.056	41.167	5.90	3.376	1.790
0.05	5.529	5.244	0.051	38.983	6.58	3.566	1.610
0.10	5.253	5.053	0.038	37.230	7.21	3.734	1.780
0.20	5.061	4.710	0.069	39.637	6.37	3.507	2.230

3.2 FTIR analysis

Figure 2a shows FTIR spectra against wave number $\bar{\nu}$ for the samples, and also the values of wave numbers $\bar{\nu}$ against absorption peaks are listed in Table 2. Firstly, there is a clear peak recorded at 3423.36, 3442.14, 3417.14, 3417.34, 3442.18 cm^{-1} , respectively, which is related to O–H stretching vibrations for ZnO (Zhao 2016; Wasly 2018). One peak is only recorded at 2924.21 cm^{-1} for the $x=0.20$ sample, but it disappears for the other samples, even for ZnO, which may be related to the solubility limit discussed above. Interestingly, the functional peak observed at 1630 cm^{-1} due to H–O–H bonding vibrations and C=C stretching, is absent for all samples (Muhammad 2019). Some other peaks were only obtained at 1426.07 and 1436.68 cm^{-1} for $x=0.00$ and 0.20. In contrast, there are also identified peaks recorded at 673.56, 672.18, 671.84, 668.13 for $x=0.00, 0.025, 0.05$ and 0.10, but it is absent for $x=0.20$. However, the presence of the peak is evidence of the incorporation of Al^{3+} ions into the ZnO matrix and corresponds to the C=C, C=O, C–N and O–H stretching and C–H bending vibration (Srinivasulu et al. 2017). Among the absorption peaks observed between (451.97–556.32 cm^{-1}) which corresponds to the active modes of ZnO related to hexagonal structure Santhosh Kumar (2017). This means that the ZnO structure is slightly different than the ideal case for $x=0.20$, as obtained from XRD analysis. This behavior indicates that Al shifted the bending and stretching vibrations of ZnO to lower values of $\bar{\nu}$, which can be attributed to the formation of a ZnAl_2O_4 bond of a longer length chain and the fact that the Al had intense ZnO and moderate metal oxide modes in the ZnO matrix structure (Raja et al. 2014).

Debye temperature θ_D is given by Ba-Abbad et al. (2013);

$$\theta_D(K) = \frac{hc \bar{\Delta\nu}}{K_B} = 1.439 \bar{\Delta\nu} \tag{1}$$

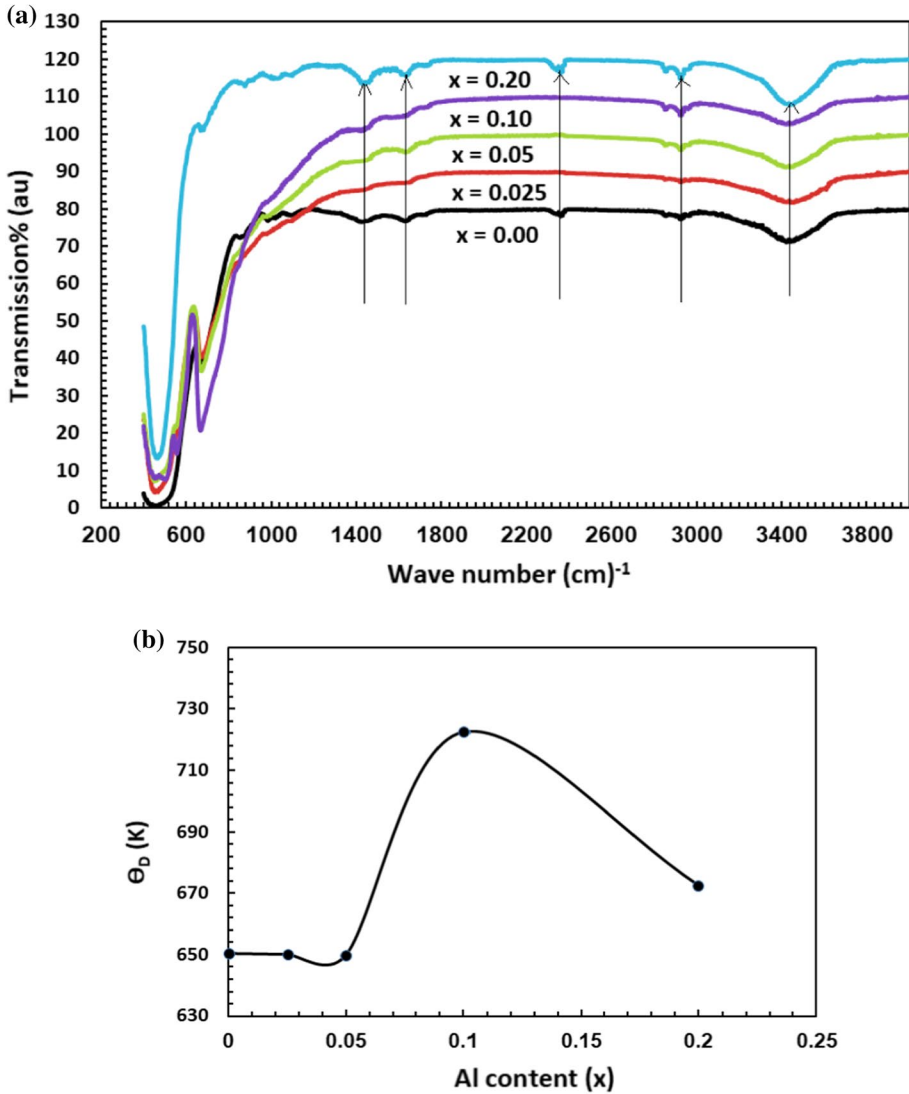


Fig. 2 **a** FTIR spectra of for pure and Al doped ZnO samples **b** Debye temperature (θ_D) versus Al content for the samples

Figure 2b shows that θ_D suddenly increases as x increases to 0.10, followed by a sudden decrease at $x=0.20$. However, this behavior is attributed to the shift in the wave number of FTIR bands to higher/lower values against x content as listed in Table 2.

The strength of the interaction between Zn cat-ions and (O^{-2}) ions of ZnO, the force constant K_t can be calculated using; $K_t=0.076W\Delta v^2$ (Santhoshkumar et al. 2017). Also, the stiffness constants S_{11} and S_{12} are easily calculated in terms of Poisson's ratio γ as; $S_{11}=(K_t/c)$, $S_{12}=(S_{11}\gamma/1-\gamma)$ and $\gamma=0.324$ (1–1.043PS) (Ahmad et al. 1456). It is

Table 2 FTIR absorption peaks, residual stress, Poisson’s ratio and elastic constants of pure and Al doped ZnO samples

$x=0.00 \nu \text{ (cm)}^{-1}$	$x=0.025 \nu \text{ (cm)}^{-1}$	$x=0.05 \nu \text{ (cm)}^{-1}$	$x=0.10 \nu \text{ (cm)}^{-1}$	$x=0.20 \nu \text{ (cm)}^{-1}$
3423.36	3442 4	3417.14	34 7.34	3442.18
2330	–	–	–	2340.21
1590	–	1610	–	1623
1426.07	–	–	1428.8	1436.68
673.56	672.18	671.84	668.13	–
–	–	–	556.32	–
–	–	–	502.43	–
452.31	452.11	451.97	–	467.76
γ				
0.304	0.305	0.307	0.311	0.301
σ(Gpa)				
–0.063	0.250	0.474	0.832	1.145
S_{11}(D/cm²)				
2.23E+11	2.23E+11	2.23E+11	2.76E+11	2.39E+11
S_{12}(D/cm²)				
9.73E+10	9.78E+10	9.86E+10	1.25E+11	1.03E+11

evident from Table 2 that ($\gamma > 0.26$) for all samples which indicates ductile nature (Mitra and Mondal 2013). The residual stress σ is calculated by El-Said Bakeer (2020);

$$\sigma = \frac{[2S_{13}^2 - S_{33}(S_{11} + S_{12})]\epsilon_{L_s}}{2S_{13}} = -232.8\epsilon_{L_s} \tag{2}$$

where S_{13} , S_{33} , S_{11} S_{12} are respectively equal 104.2, 213.8, 208.8 and 119.7 GPa for ZnO (Mazen et al. 2007). As listed in Table 2, σ is negative (compressive-like behavior) for ZnO. In contrast, it is positive (tensile-like behavior) for the doped samples, indicating that Al was able to eliminate the compressive stress of ZnO and turn it into tensile stress. This may be related to the number of pores and the lattice defects discussed above (Anupama et al. 2017). Young Y, bulk modulus β and rigidity modulus G are determined by Modi et al. (1543); MariemChaari and matoussi et al., 2011);

$$Y = \frac{(S_{11} - S_{22}(S_{11} + 2S_{12}))}{(S_{11} + S_{12})}; \beta = \frac{S_{11} + 2S_{12}}{3}; G = \frac{Y}{2(\gamma + 1)} \tag{3}$$

As shown in Fig. 3, both of them are increased as x increased to 0.10, followed by a decrease at x=0.20. This increase may be related to the shrinkage of inter-atomic bond length L which subsequently controls the ZnO bond strength (Rao et al. 2010).

3.3 Optical measurements

As shown in Fig. 4a-b, the relationship between reflectance/absorption (R/A) and wave lengths reveals two minimum/maximum regions for all samples at about 400 nm, which may be related to increasing free carrier density in the near-UV region (Rusu et al. 2011).

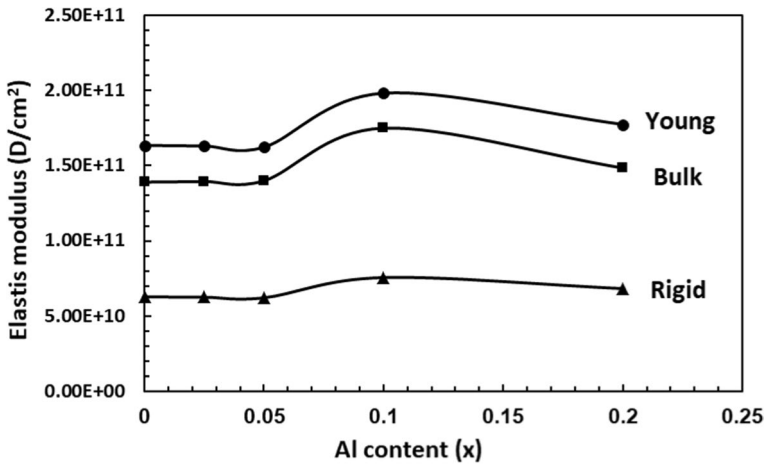


Fig. 3 Elastic modulus (Y,B,G) versus Al content for the samples

Interestingly, the change in (R/A) for Al-doped samples is related to the oxygen vacancies, which usually make ZnO suitable for gas sensors (Patange et al. 2013; Rajesh Babu and Tatarchuk 2018). As given in Table 3, the first A_{\max} or R_{\min} occurs at $(\lambda (1)_{\max} = 314 \text{ nm})$ for all samples, while the second A_{\max} or R_{\min} occurs at $\lambda (2)_{\max} = 352, 364, 350, 344$ and 346 nm , respectively. Therefore, first exciton energy $E_{\text{ex}}(1)$ is 3.953 eV for all samples, while the second exciton $E_{\text{ex}}(2)$ is decreased for $x=0.025$, followed by an increase to $x=0.20$. This means that the required energy for creating electron-hole pairs is decreased by 0.025 of Al, followed by an increase of up to 0.20 . Generally, E_{ex} of ZnO is the required photon energy for electronic transition from the VB of (O-2p) to the (Zn-3d) of CB to form an exciton bound state (e-h) of 100 meV of binding energy and energy close to E_g . The (e-h) are usually held together by the electrostatic Coulomb force and they have kinetic energy and a narrow spectrum, which is highly attractive for laser devices if we can trap the excitons and reduce their motion, which further narrows the energy spread (Chen and Li 2019, Rodnyi et al. 2018b, Al Naim and Sedqi 2021).

The absorption coefficient α is calculated by, $\alpha = 2.303 \ln (A/t)$, and the optical band gap E_g is obtained using Taucs equation (Ali et al. 2005; Chen and Li 2019);

$$(\alpha h\nu)^{\frac{1}{m}} = A(h\nu - E_g) \quad (4)$$

m represents the transition in the semiconducting materials and has values of $1/2$ and 2 for allowed direct and indirect transitions, respectively, and B is a constant, and t is the diameter of the glass cuvette. The plot of $(\alpha h\nu)^2$ against the photon energy is used to get the value of the E_g (see Fig. 5). As shown in the figure, two absorption edges are observed for all samples, indicating that there are two direct electronic transitions due to the absorption of the photon energy. The values of E_g are obtained from the Figure are summarized in Table 3. The first (E_{gh}) is obtained at UV region, while the second one (E_{gl}) is obtained in the visible region. The values of E_{gh} and E_{gl} are $3.60, 3.56, 3.43, 3.53, 3.68 \text{ eV}$ and $3.02, 2.95, 2.85, 2.92, 3.07 \text{ eV}$ respectively. This suggests both E_{gh} , and E_{gl} had similar behavior as the x increased to 0.20 . It is also evident from Table 2 that $\Delta E = (E_{\text{gh}} - E_{\text{gl}})$ is $0.58, 0.61, 0.58$ and 0.61 eV for all samples, in which ΔE is constant. Anyhow, two E_g are also

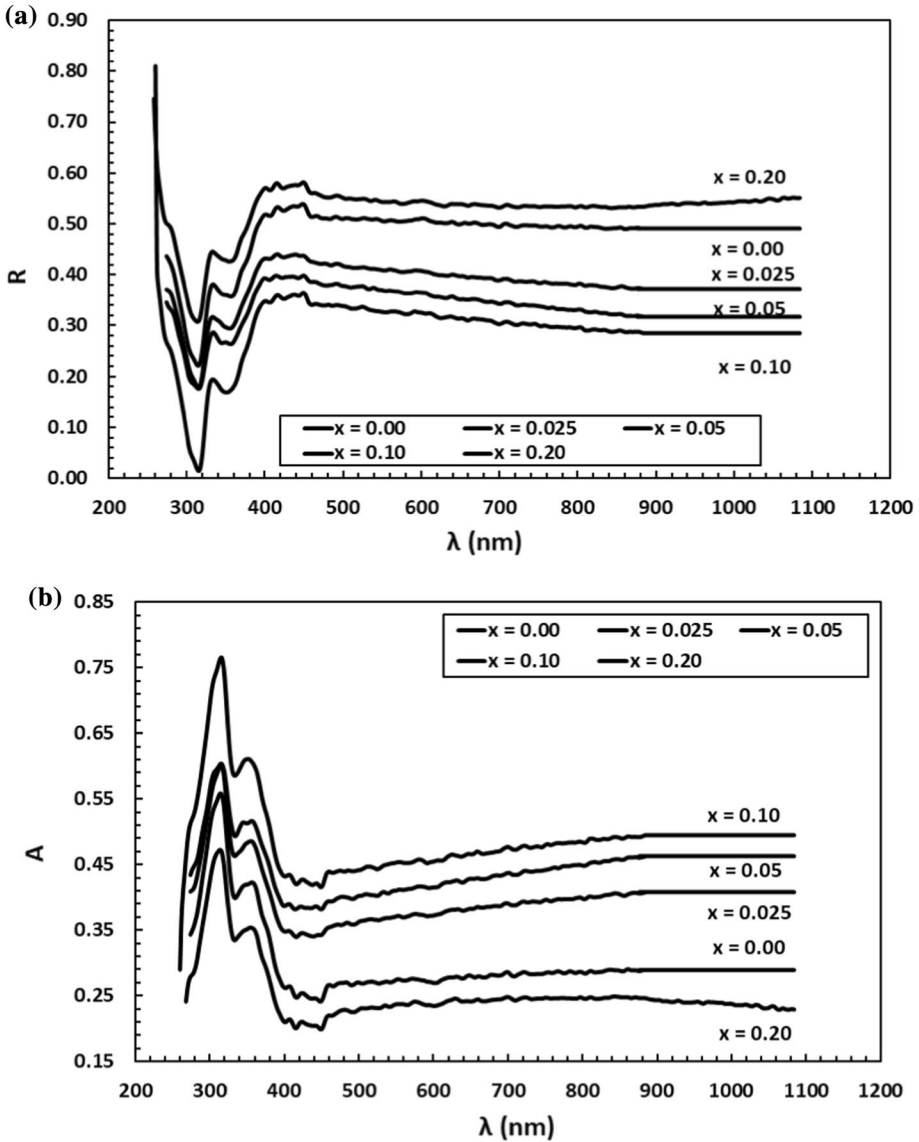


Fig. 4 a Reflectance (R) versus wave length for pure and Al doped ZnO samples b Absorption (A) versus wave length for pure and Al doped ZnO samples

recorded for n-type semiconductors (Rodnyi et al. 2018b; Al- and Naim and Sedky, 2021; Mukhtar et al. 2012). In that case, the doping of ZnO with Al may produce a high carrier concentration and, as a result, more conduction band energy states are formed, which, in turn, reduces the E_g as obtained. However, the further increment of E_g above $x = 0.05$ may be due to the formation of structural defects in the host materials, thereby creating insulating states in the forbidden gap inside the band structure, and therefore, E_g was slightly increased.

Table 3 λ , E_{ex} , E_{eg} , ϵ_L , (N/m^3) , N and R for the samples

x	$\lambda(1)_{\text{max}}$ (nm)	$\lambda(2)_{\text{max}}$ (nm)	$E_{\text{ex}}(1)$ (eV)	$E_{\text{ex}}(2)$ (eV)	E_{eg} (eV)	E_{gl} (eV)	ϵ_L	$(N/m^3) \times 10^{24}$ ($\text{g}\cdot\text{cm}^{-3}$)	$R \times 10^{-11}$ (cm)
0.00	314	352	3.953	3.526	3.60	3.02	8.78	2.64	8.77
0.025	314	364	3.953	3.410	3.56	2.95	5.06	3.01	8.40
0.05	314	350	3.953	3.547	3.43	2.85	4.04	3.51	7.98
0.10	314	344	3.953	3.608	3.53	2.92	3.48	3.81	7.76
0.20	314	346	3.953	3.588	3.68	3.07	9.37	18.45	4.59

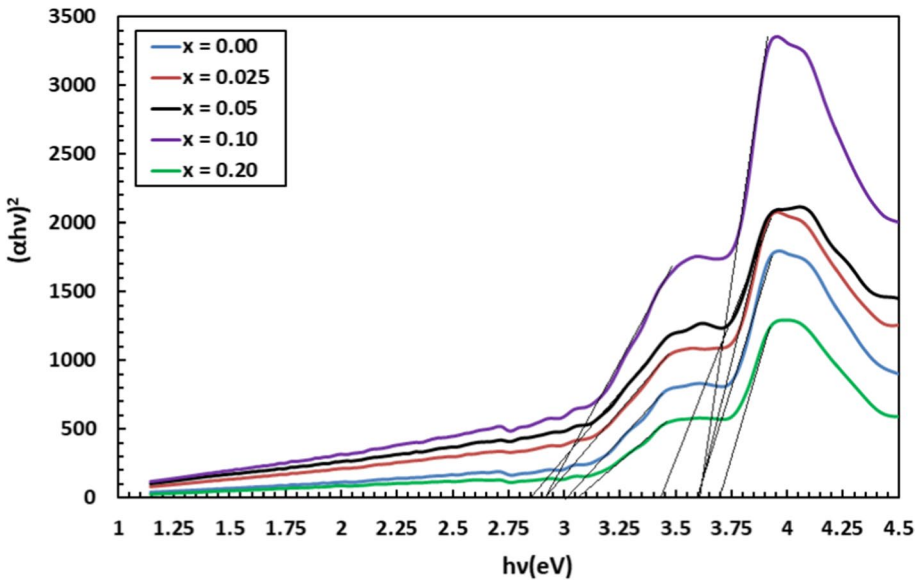


Fig. 5 $(\alpha hv)^2$ versus photon energy for pure and Al doped ZnO samples

In addition, the high frequency dielectric constant of $Zn_{1-x}Al_xO$ is calculated from the following relation, which represents the dependence of the refractive index n on the wavelength λ (Othman et al. 2017; Ismail et al. 2011a);

$$n^2 = \epsilon_L - \left(\frac{e^2}{4\pi^2 c^2 \epsilon_0} \right) \left(\frac{N}{m^*} \right) \lambda^2 \tag{5}$$

where c , e , m^* , ϵ_L and N denote light speed, electron charge, free space permittivity, effective mass of electron, residual lattice dielectric constant, and free carrier concentration, respectively. The intercept and slope of the straight lines in Fig. 6 give the values of ϵ_L and N/m^* , which are listed in Table 3, are slightly increased by x up to $x=0.10$, followed by a sharp increase at $x=0.20$, whereas ϵ_L is decreased to $x=0.10$, followed by a sharp increase at $x=0.20$. The inter-atomic distance (R) given by $(0.86/N)^{(1/3)}$ (Abdel-Khalek et al. 2019) and listed in Table 3 decreases as x increases to 0.20. Based on the above results, the higher valence state of the Al^{3+} compared to Zn^{2+} led to slightly deeper donors and, consequently, more carriers were generated. Furthermore, and in parallel, the ability of electron migration may be enhanced (Ismail et al. 2011b). Furthermore, Al is nearly non-magnetic, and the addition of Al beside Zn will decrease the localization of the carriers. Therefore, we strongly recommend the Al doped samples for optoelectronic applications.

3.4 Dielectric measurements

The real ϵ' part of the sample dielectric constant is determined by using the relation (El-Denglawey and El-Denglawey 2018; Sagadevan et al. 2017);

$$\epsilon' = \frac{Cd}{\epsilon_0 A} \tag{6}$$

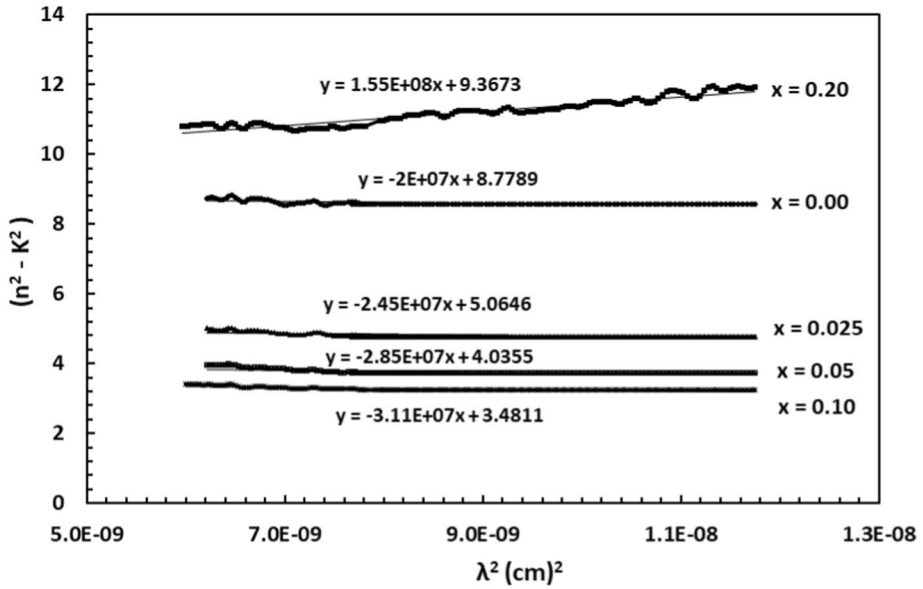


Fig. 6 Real part of optical dielectric constant (n^2-k^2) against wave length for pure and Al doped ZnO samples

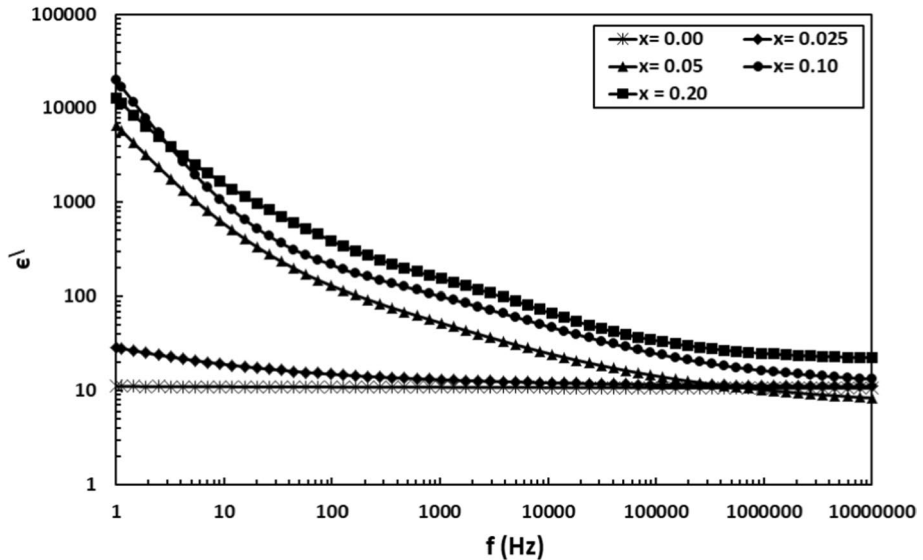


Fig. 7 Dielectric constant (ϵ') versus frequency for pure and Al doped ZnO samples

where C is the capacitance of the sample and C_0 is the empty cell capacitance ($C_0 = \epsilon_0 A/d$), d is the sample thickness, A is the surface area of the electrodes, $\epsilon_0 = 8.85 \times 10^{-12}$ (F/m) is the permittivity of free space. Figure 7 shows the plot of ϵ' against f for all samples. It is clear that ϵ' is gradually decreased as f increases up to 10^4 Hz for all samples, and above

that it decreases, then saturated at 10^7 Hz. In addition, it is slightly increased as x increases up to 0.025, but there is a significant increase with a further increase of x above 0.025. For example, ϵ' of $x=0.20$ is at least about 10^3 times that of $x=0.00$, which indicates that the addition of Al above 0.025 to Zn shifts the dielectric medium to higher values. Therefore, when a field is applied, the charge carriers can easily move within the grains at a low f below 10 MHz, but they are accumulated at the grain boundaries, resulting in the large interfacial polarization, and, in turn, high ϵ' . With a rise in frequency above 10 MHz, a decrease of ϵ' could be obtained. This is due to the fact that any species contributing to polarization is found to lag behind the applied field, and consequently, the dipoles cannot follow the ac field (Abdel-Khalek et al. 1178; Hazem Mahmoud Ali and Ahmed Mohamed Abdel Hakeem 2015; Selvakumar et al. 2014). On the other hand, the increase of ϵ' with x can be explained in terms of increasing electro-negativity between Al and O, which is 1.83 instead of 1.79 between Zn and O, and also increasing the number of carriers as indicted above (Mehedi Hassan et al. 2015; Singh et al., 2015). Due to this, the strength of the Al-O ionic bond is improved, which results in an increase in the dielectric polarization. Moreover, the decrease in crystallite size and average crystalline size leads to an increase in the number of dipoles, which results in a decrease in polarization and increases the ϵ' values for the doped samples, as reported (Zamiri et al. 2014a).

The total conductivity can be obtained by Zamiri et al. 2014b;

$$\sigma_t(\omega) = \sigma_{dc} + \sigma_{ac} = \sigma_{dc} + B\omega^s \tag{7}$$

where σ_{dc} is the dc conductivity calculated at zero f , B is constant, and s is the exponent of frequency. Figure 8 shows the real part (σ') of σ_{ac} as a function of f . It is evident from the figure that σ' gradually increases by increasing f for all samples up to 10 MHz, obeying the universal power law (Singh and Singh 2020a). In addition, σ' for Al-doped samples is higher than that of ZnO due to the increased charge carriers through the replacement

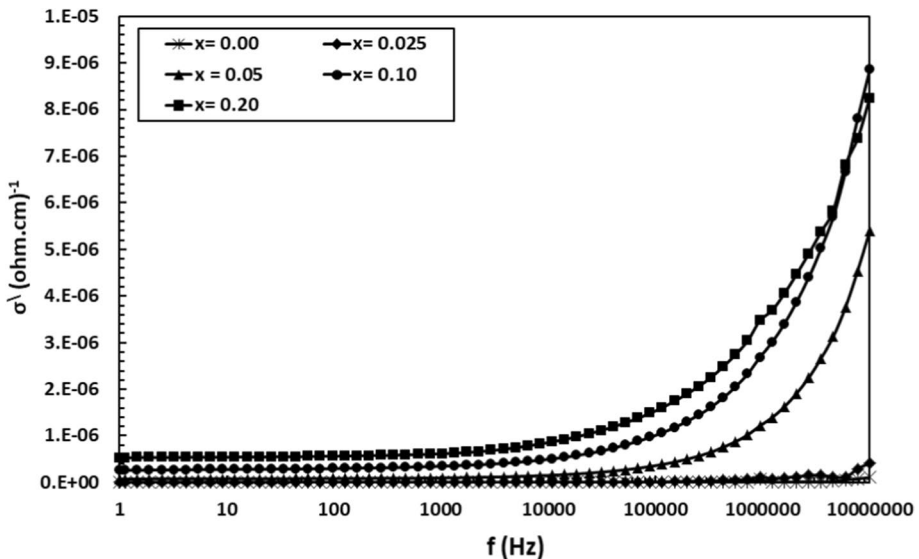


Fig. 8 Ac conductivity (σ') versus frequency for pure and Al doped ZnO samples

of Zn^{2+} by Al^{3+} . At low f , the field drift carries over a large distance, and therefore σ' is almost unchanged. As f is raised, the displacement of carriers is reduced, and at a critical frequency ω_p , σ' follows the relation; ($\sigma_{ac} \sim \omega^s$) with ($0 \leq s \leq 1$) for hopping conduction (Saadi et al. 2020). These outcomes indicate that the addition of Al supports the σ_{ac} of ZnO as obtained.

However, the linear fit between $\ln \sigma'$ and $\ln \omega$ shown in Fig. 9a,b gives two different linear regions. The obtained values of s and B at low and high frequencies, designated as s_L , s_h , B_h and B_L are obtained and listed in Table 4. The values of s_L are between 0.565, 0.898

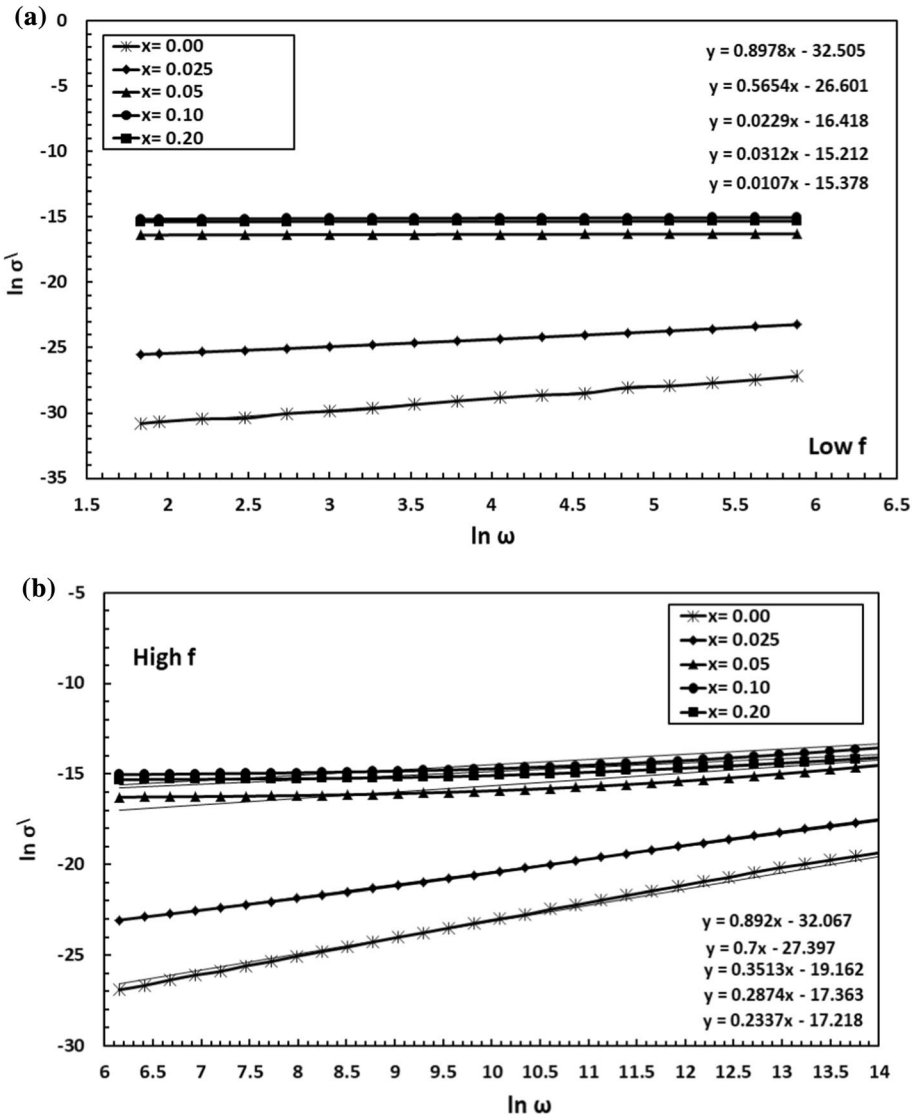


Fig. 9 a $\ln \sigma'$ versus $\ln \omega$ at low frequency for pure and Al doped ZnO samples b $\ln \sigma'$ versus $\ln \omega$ at high frequency for pure and Al doped ZnO samples

Table 4 σ_{dc} , S , B and W_m for pure and Al doped ZnO samples

Al content x	σ_{dc} ($\Omega.cm$) ⁻¹	s_L	s_h	B_L	B_h	W_{mL} (eV)	W_{mh} (eV)
0.00	3.E-11	0.898	0.892	7.64E+15	1.18E+14	1.520	1.435
0.025	2.E-10	0.565	0.700	2.80E+12	1.26E+12	0.356	0.517
0.05	8.E-08	0.023	0.351	7.41E+08	4.76E+09	0.159	0.239
0	7.E-08	0.031	0.287	2.43E+07	2.88E+08	0.160	0.217
0							
0.20	6.E-08	0.011	0.234	2.10E+07	3.33E+08	0.157	0.202

for $x=0.00$ and 0.025 samples, which indicates electronic conduction. But with increasing x above 0.025 , the values of s_L are $0.023, 0.031, 0.011$, which indicates hole conduction. However, similar behavior is obtained for s_h . This behavior is attributed to the excess number of hole carriers which may be generated as a result of the difference between Zn^{2+} and Al^{3+} .

According to correlated barrier hopping (CBH) model, the binding energy W_m , is given by Samanta et al. (2020);

$$s = 1 - \frac{6K_B T}{W_m + K_B T \ln \omega \tau_0} = 1 - \frac{6K_B T}{W_m} \tag{8}$$

where τ_0 is the characteristic relaxation time and is in the order of the atomic vibration of 10^{-13} s. The values of W_m correlated with the range of f are listed in Table 4. Although they are decrease with x , the $W_{mh} \approx 1.5 W_{mL}$ except for $x=0.00$ in which $W_{mh} \approx 0.94 W_{mL}$. In addition, the minimum hopping distance (R_{min}) is given by Samanta et al. (2020);

$$R_{min}(\omega) = \frac{e^2}{\pi \epsilon_0 \epsilon \sqrt{W_m + K_B T \ln \omega \tau_0}} \sim \frac{e^2}{\pi \epsilon_0 \epsilon \sqrt{W_m}} \tag{9}$$

where $\bar{W}_m = [(W_{mL} + W_{mh})/2]$. On the other hand, the density of localized states at which carriers exist N can be expressed by Samanta et al. (2020);

$$N(\omega) = \frac{24\sigma^{\lambda}}{\pi^3 \epsilon_0 \epsilon \sqrt{\omega} R_{min}^6} \tag{10}$$

As shown in Fig. 10a, the unusual behavior of R_{min} can be classified into two series relative to $x=0.00$. The vice is versa for the behavior of $N(\omega)$ against the x , see Fig. 10b. These results indicate that the R_{min} mechanism against f is controlled by the x in the low under doped region ($x=0.025$) and also in the over-doped region ($x=0.20$).

In addition, the density of states at Fermi level $N(E_f)$ can be calculated by Singh et al. (1832);

$$N_{E_f}(\omega) = \sqrt{\frac{3\sigma^{\lambda} \alpha^5}{4e^2 \omega K_B T (\ln \frac{10^{13}}{\omega})^2}} \tag{11}$$

where α is the localized wave function and equals $10^{10} m^{-1}$ and $f_0 = 10^{13}$ Hz is the photon frequency corresponding to the applied ac field. However, the behavior of $N(E_f)$ against x shown in Fig. 11a seems to be systematic because $N(E_f)$ is gradually increased as x increases to 0.20 . But it has unusual behavior against f where it gradually increases for

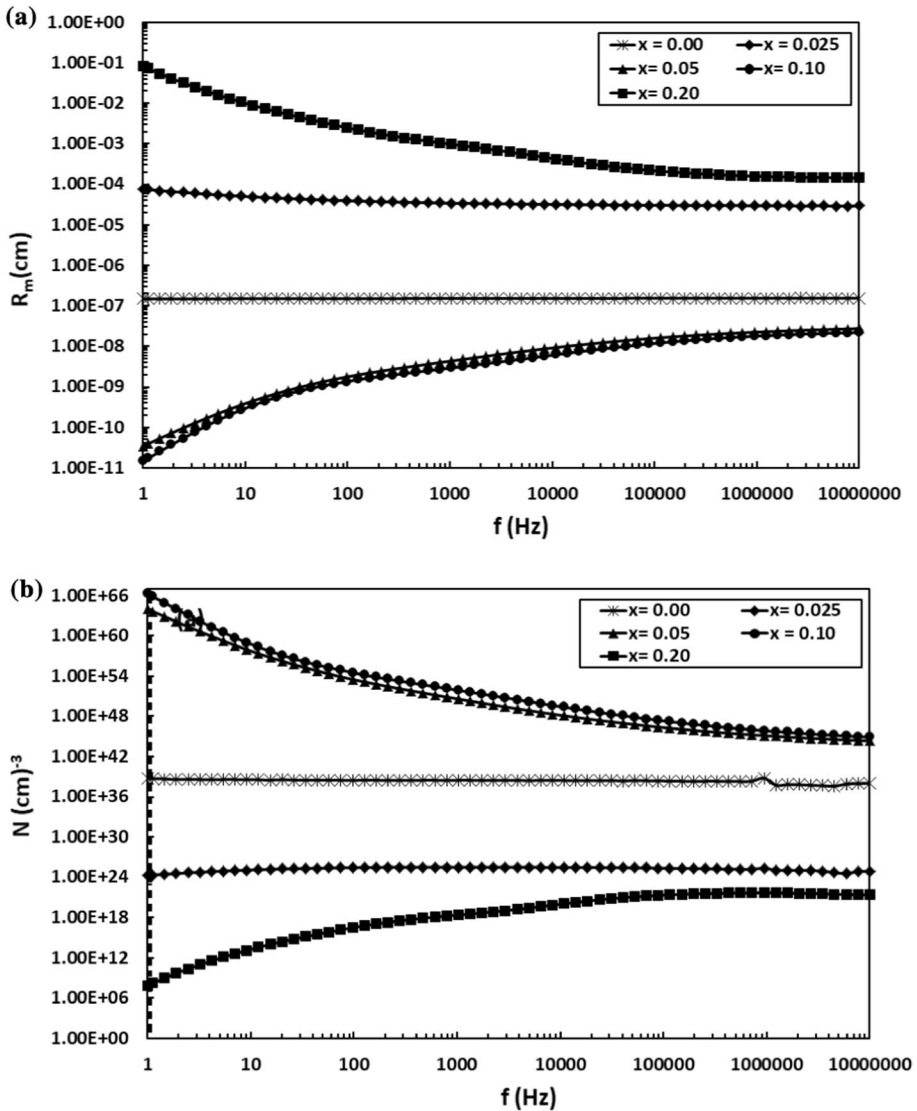


Fig. 10 **a** Hopping distance (R_{\min}) versus frequency for pure and Al doped ZnO samples **b** Density of localized states (N) versus frequency for pure and Al doped ZnO samples

$x=0.00$ and 0.025 samples, goes to an optimum, and then decreases. But with increasing x above 0.025 , $N(E_F)$ decreases, increases and goes to an optimum and then decreases. The increase in $N(E_F)$ against x confirms the increase in σ_{ac} , and may support the growing concentration of defect energy states in ZnO (Zeyada et al. 2016). Our interesting point here is the optimum values of $N(E_F)$ obtained at about 195 kHz for all samples and also its dependence on x . For example, $N(E_F)$ was increased from 8.05×10^{19} $(\text{erg}\cdot\text{cm}^3)^{-1}$ for $x=0.00$ to 2.01×10^{20} , 8.97×10^{20} , 1.75×10^{21} and 1.78×10^{21} $(\text{erg}\cdot\text{cm}^3)^{-1}$ for the doped samples, respectively. This behavior is not clear to us at present and may be either related

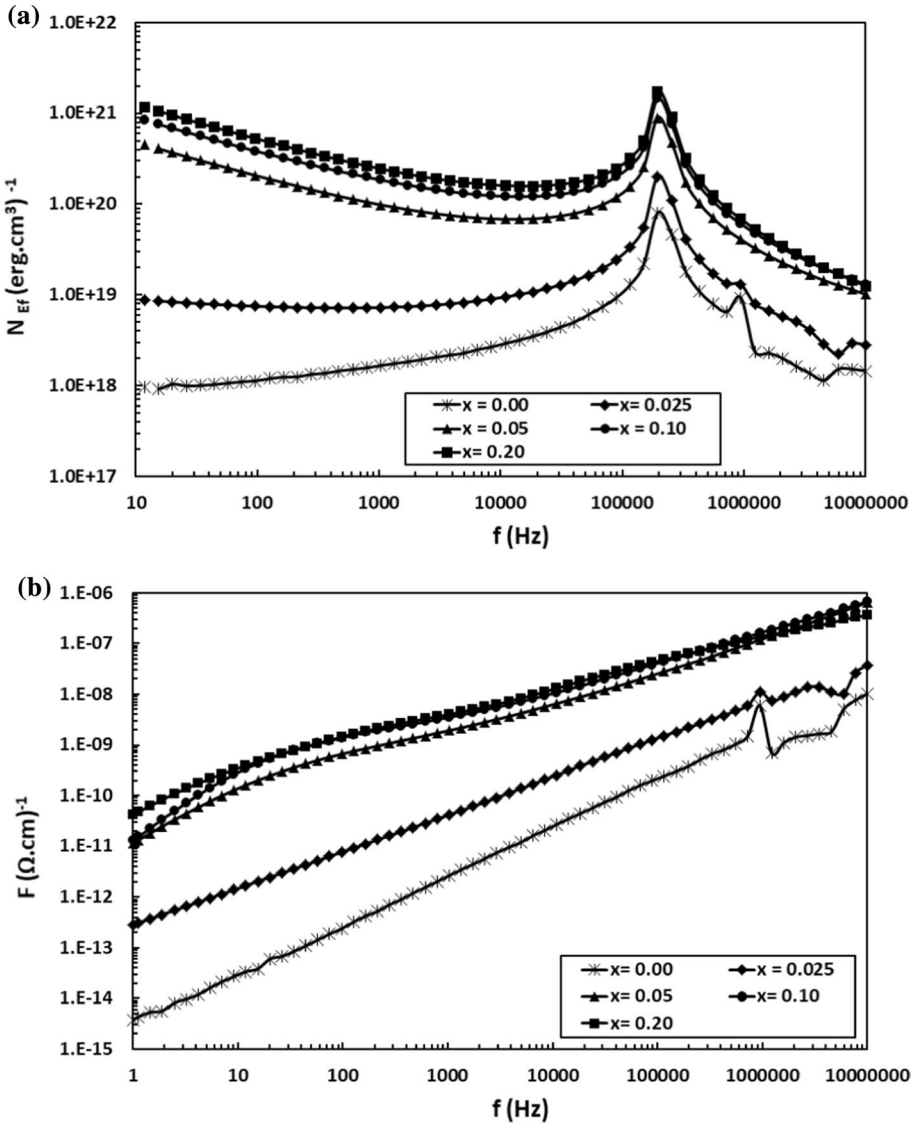


Fig. 11 **a** Density of states at the Fermi level $N(E_f)$ versus frequency for pure and Al doped ZnO samples **b** F-factor versus frequency for pure and Al doped ZnO samples

to the resonance of lattice vibrations against ac field/or the enhancement of ac conductivity at 195 kHz. The higher value of F , as a figure of merit given by, $(\sigma_{ac}/\epsilon^{\prime})$ is mainly a good indicator for a sample to be more suitable for solar cell applications (Loane et al. 1991; Elliott 1987). As shown in Fig. 11b, the F factor is gradually increased by increasing x , but it is almost constant above $x=0.05$. These results strongly recommend the Al doped samples up to $x=0.10$ for solar cell design.

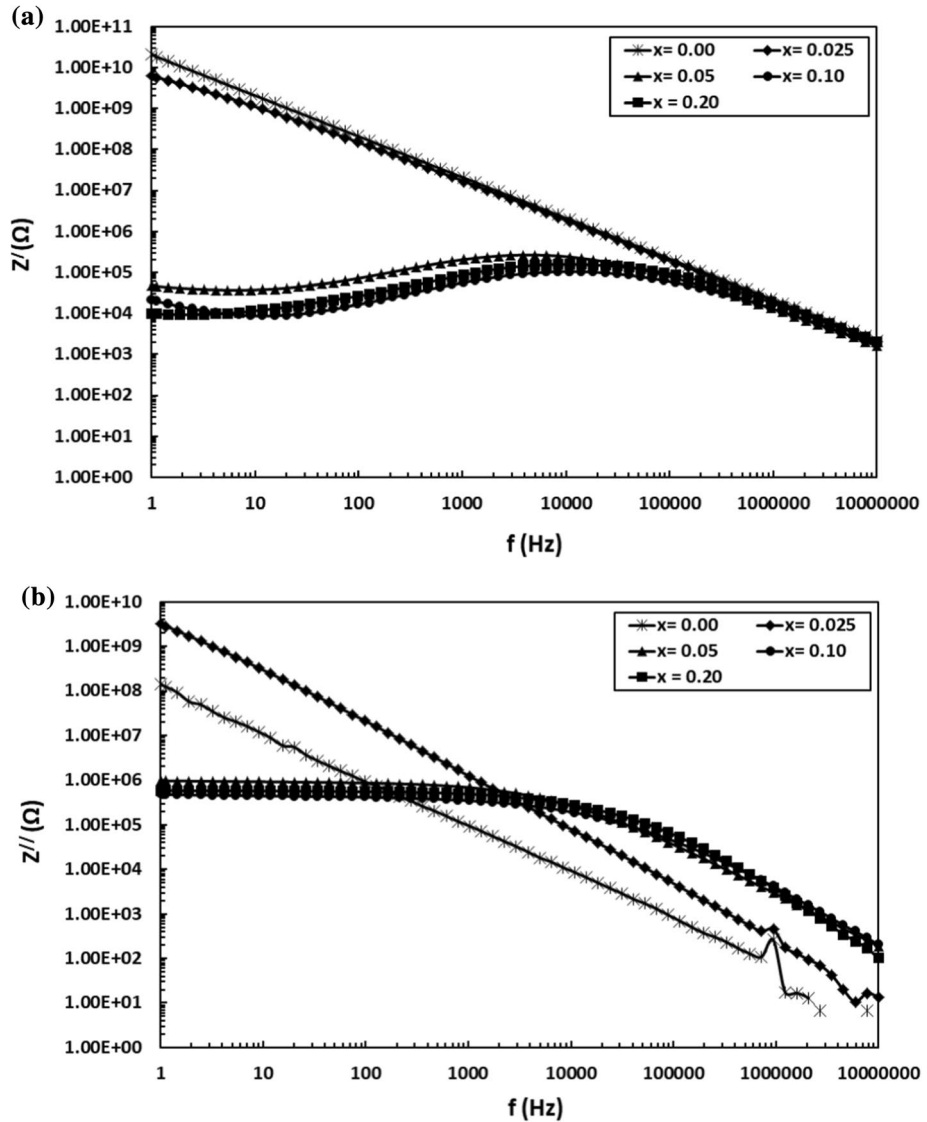


Fig. 12 a Impedance (Z) versus frequency for pure and Al doped ZnO samples b Impedance ($Z//$) versus frequency for pure and Al doped ZnO samples

Figure 12a, b shows the variations of Z and $Z//$ against f for all samples. It is evident that Z and $Z//$ for $x \leq 0.025$ samples are decreased linearly as a straight line with a rise in f . In addition, Z was also decreased as x increased, whereas $Z//$ was increased. With a further increase of x above 0.025, Z is slightly increased with f and goes to higher values at about 10 kHz, and then decreases at 10 MHz. It also decreases as x increases below 100 kHz, but above that it is nearly constant for all samples. In contrast, a little bit of a decrease is obtained below 10 kHz for $Z//$ against f followed by a significant increase with the rise in f to 10 MHz, but it becomes higher than that of $x \leq 0.025$ samples. However, the increases

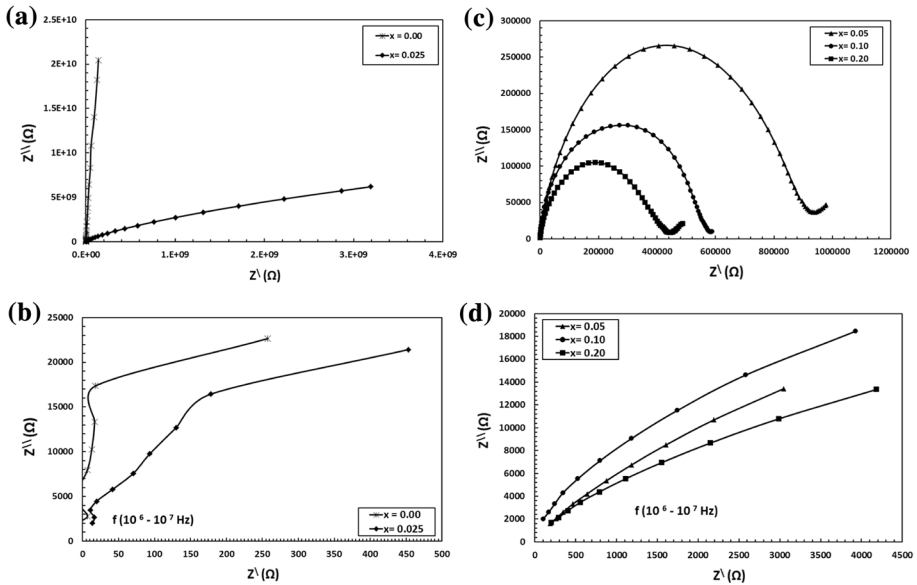


Fig. 13 **a** Cole- Cole plot for $x=0.00$ and 0.025 samples **b** Cole- Cole zoom at high frequencies for $x=0.00$ and 0.025 samples **c** Cole- Cole plot for $x=0.05, 0.10$ and 0.20 samples **d** Cole- Cole zoom at high frequencies for $x=0.05, 0.10$ and 0.20 samples

in Z at low f confirm the highly resistive grain boundaries, whereas the decrease is due to the rise in the hopping of charge carriers (Sedky et al. 2022b; Cherifi 2016). Anyhow, the Cole- Cole plot and also the zoom at high frequencies are shown in Fig. 13a-d and the impedance of grains and grain boundaries is determined at the half and end of the semi-circle-shape plot, respectively. It is evident that the impedance spectra of $x=0.00$ sample is straight line like- shape with $Z^{\prime}=2.05 \times 10^{10} \Omega$ and $Z^{\prime \prime}=1.39 \times 10^8 \Omega$. With increasing x to 0.025 , it becomes half semicircle (one quarter) like-shape, and with more increase of x to 0.05 , a complete semicircle like-shape with a large radius is obtained. Similar behavior is also obtained for $x \geq 0.10$, but the area of the semicircle is gradually decreased as x increases. However, the values of the impedance of grain and grain boundaries for all doped samples $Z^{\prime}(g), Z^{\prime}(gb), Z^{\prime \prime}(g)$ and $Z^{\prime \prime}(gb)$ are listed in Table 5, in which they are gradually decreased as x increases to 0.20 .

It can be seen that the frequency used for a pure sample is insufficient to cover the grain boundary, and thus the $Z(g)$ and $Z(gb)$ cannot be calculated. The $Z(gb)$ was reduced by increasing x to 0.025 , and the frequency was able to make it as one quarter of a circle because

Table 5 Impedance resistance (Z^{\prime} and $Z^{\prime \prime}$) for grain and grain boundaries of pure and Al doped ZnO samples

x	$Z^{\prime}(g)$ (Ω)	$Z^{\prime \prime}(g)$ (Ω)	$Z^{\prime}(gb)$ (Ω)	$Z^{\prime \prime}(gb)$ (Ω)
0.00	–	–	–	–
0.025	3.19×10^9	6.19×10^9	6.38×10^9	4.92×10^8
0.05	4.59×10^5	2.65×10^5	10.02×10^5	4.15×10^4
0.10	3.01×10^5	1.65×10^5	6.01×10^5	1.56×10^4
0.20	1.88×10^5	1.05×10^5	4.41×10^5	1.13×10^4

the $Z(\text{gb})$ was reduced, and it can be obtained approximately. With an increase in x above 0.025, the applied frequency is more than adequate for covering the grain boundary, allowing the $Z(\text{g})$ and $Z(\text{gb})$ to be calculated. However, a single arc of an identical $\tau = (1/\omega) = RC$ has been obtained in pure and doped ZnO (Ramesh Babu et al. 2012; Giuntini et al. 1981). Because of this behavior, conduction in grains and their boundaries could not be separated (Fahim et al. 2018). Other reports believed that a single arc was caused by the combined contributions of the grain's core resistive and grain boundary (Singh and Singh 2020b). This fact suggests that the excess of doping probably exists in the grain boundary region, either as a very thin secondary phase, which could benefit the grain boundary transport for grain growth (Elkar et al. 2018).

4 Conclusion

Structural, FTIR, optical and dielectric properties of $\text{Zn}_{1-x}\text{Al}_x\text{O}$ were investigated. Regardless of the $x=0.20$ sample, which shows unusual behavior, the lattice constants, crystallite diameter, porosity, and average crystalline size are decreased by Al, while the Debye temperature and elastic modulus are increased. The residual stress is compressive for the ZnO, but it is tensile for the doped samples. Although two different values of E_g are apparent for each sample, the $\Delta E = (E_{g_h} - E_{g_l})$ between them is almost constant. Further, the residual dielectric constant is decreased as x increases to 0.10, followed by a sharp increase at $x=0.20$, while the opposite behavior is obtained for (N/m^*) . The conduction is electronic for $x \leq 0.025$ samples, but it is changed to hole for $x > 0.025$. Although W_m decreased by increasing x , there was no exact trend for the behaviors of R_{\min} and N against x . Interestingly, $N(E_F)$ has an optimum value at 195 kHz for all samples. The F-factor for solar cell design is increased as x increases to 0.10, but it is almost constant at $x=0.20$. The Cole–Cole plot for the samples is a straight line for $x=0.00$, a semicircle arc for $x=0.025$, and a complete semicircle for $x \geq 0.05$. The $Z'(G)$ and $Z'(GB)$ are gradually decreased by increasing x to 0.20. These outcomes strongly recommend the AlZnO samples for the design of optoelectronic and solar cell instruments.

Acknowledgements The authors extend their appreciation to the Deanship of Scientific Research at King Khalid University for funding this work through research groups program under grant number R.G.P.2/151/43. They are also thanking KFU Saudi Arabia for cooperation during dielectric measurements.

Funding This article was supported by King Khalid University, 2/151/43, Atif Mossad Ali

Declarations

Conflict of interest The authors declare that they have no competing interests and the present work is original not published or submitted for evaluation to another Journal. Moreover, the obtained systematic findings or study strongly recommend the Al doped samples for advanced applications such as Optoelectronic and solar cell instruments, which probably have never been early reported elsewhere over the last 3-years, which and highlight the present investigation. In addition, the datasets generated during and/or analyzed during the submitted current study are only available from the corresponding author on reasonable request.

References

Abdel-Khalek, H., Shalaan, E., El Salam, M.A., El-Sagheer, A.M., El-Mahalawy, A.M.: Effect of thermal annealing on structural, linear and nonlinear optical properties of naphthalene tetracarboxylic dianhydride thin films. *J. Mol. Struct.* **1178**, 408–419 (2019)

- Abdel-Khalek, H., Shalaan, E., Abd- El Salam, M., El-Sagheer, A.M., El-Mahalawy, A.M.: Effect of thermal annealing on structural, linear and nonlinear optical properties of 1, 4, 5, 8-naphthalene tetracarboxylic dianhydride thin films. *J. Mol. Struct.* **1178**, 408–419 (2019)
- Ahmad, M.M., Mushtaq, S., Al Qahtani, H.S., Sedky, A., Alam, M.W.: Investigation of TiO₂ nanoparticles synthesized by Sol-Gel method for effectual photodegradation. *Oxid. Reduct. React. Cryst.* **11**, 1456 (2021)
- Al Naim, A.F., Sedky, A.: Superconductivity and Thermal Fluctuation of Y1-x Mx 123 systems with (M = Pr, Ca) & (0.00 ≤ x ≤ 0.50): Comparative Study. *Physica B* **621**, 413288 (2021)
- Al-Naim, A.F., Sedky, A., Afify, N., Ibrahim, S.S.: Structural, FTIR spectra and optical properties of pure and co-doped Zn1-xyFexMyO ceramics with (M= Cu, Ni) for plastic deformation and optoelectronic applications. *Appl. Phys. A* **127**(11), 1–20 (2021)
- Ali, H.M., Hakeem, A.M.A.: Characterization of n and p-type (SnO₂)x(ZnO)1-x nanoparticles thin films. *Eur. Phys. J. Appl. Phys.* **72**(1), 10301–10308 (2015)
- Ali, H.M., Mohamed, H.A., Mohamed, S.H.: Enhancement of the optical and electrical properties of ITO thin films deposited by electron beam evaporation technique *Eur. Phys. J. Appl. Phys.* **31**, 87 (2005)
- Aljaafari, A. A., Sedky, A.: Influence of fine crystal percentage on the electrical properties of ZnO ceramic-based varistors. *Crystals* **10**, 681 (2020)
- Alzaid, M., Hadia, N.M.A., Shaaban, E.R., El-Hagary, M., Mohamed, W.S.: Drive towards sonochemically synthesized ternary metal sulfide for high-energy supercapattery. *Energy Technol* **9**(11), 2100110 (2022)
- Amin, S.A., Sedky, A.: On the correlation between electrical, optical and magnetic properties of Zn_{1-x}Pr_xO nanoparticles. *Mater. Res. Express* **6**, 065903 (2019)
- Anupama, A.V., Rathod, V., Jali, V.M., Sahoo, B.: Composition dependent elastic and thermal properties of Li-Zn ferrites. *J. Alloys Compd.* **728**, 1091–1100 (2017)
- Arda, L., Ozturk, O., Asikuzun, E., Ataoglu, S.: Structural and mechanical properties of transition metals doped ZnMgO nanoparticles. *Power Tech.* **235**, 479–484 (2013)
- Attia, A.A., Soliman, H.S., Saadeldin, M.M., Sawaby, K.: AC electrical conductivity and dielectric studies of bulk p-quaterphenyl. *Synth. Met.* **205**, 139–144 (2015)
- Ba-Abbad, M.M., Kadhum, A.A.H., Mohamad, A.B., Takriff, M.S., Sopian, K.: The effect of process parameters on the size of ZnO nanoparticles synthesized via the sol-gel technique. *J. Alloy. Compd.* **550**, 63–70 (2013)
- Belkhaoui, C., Mzabi, N., Smaoui, H., Daniel, P.: Enhancing the structural, optical and electrical properties of ZnO nanoparticles through (Al + Mn) doping. *Results Phys.* **12**, 1686–1696 (2019)
- Brankoviz, Z., Brankoviz, G., Poleti, D., Varela, A.J.: Structural and electrical properties of ZnO varistors containing different spinel phases. *Ceram. Int.* **271**, 115–122 (2001)
- Chaari, M., Matoussi, A., Fakhfakh, Z.: Structural and dielectric properties of sintering zinc oxide bulk ceramic. *Mater. Sci. Appl.* **2**(7), 764 (2011)
- Chen, H., Tang, Y., Jaing, T., Li, G.: in *Comprehensive Nanoscience and Nanotechnology (Second Edition)*, Academic Press **1**, 305–318 (2019)
- Cherifi, Y., Chaouchi, A., Lorgoilloux, Y., Rguiti, M.: Electrical, dielectric and photocatalytic properties of Fe-doped ZnO nanomaterials synthesized by sol gel method. *Process. Appl. Ceramics* **10**(3), 125–135 (2016)
- Das, S., Das, S., Sutradhar, S.: Enhanced dielectric behavior and ac electrical response in Gd-Mn-ZnO nanoparticles. *Alloys Comp.* **726**, 11–21 (2017)
- Deng, J., Zheng, H., Zheng, X., Yao, M., Li, Z. and Gao, C.: Gold nanoparticles with surface-anchored chiral poly(acryloyl-L(D)-valine) induce differential response on mesenchymal stem cell osteogenesis *Nano Res.* **9**, 3683–3694 (2016)
- Djerdj, I., Jaglici, Z., Arcon, D., Niederberger, M.: Co-doped ZnO nanoparticles: minorreview. *Nanoscale* **2**, 1096–1104 (2010)
- El-Denglawey, A., El-Denglawey, A.: Illumination effect on the structural and optical properties of nano meso nickel (II) tetraphenyl-21H, 23H-porphyrin films induces new two hours photo bleached optical sensor. *J. Lumin.* **194**, 381–386 (2018)
- Elkar, T., Mzabi, N., Ben Hassine, M., Gemeiner, P., Dkhil, B., Guermazi, S., Guermazi, H.: Structural and optical investigation of (V, Al) doped and co-doped ZnO nanopowders: tailored visible luminescence for white light emitting diodes. *Superlattice. Microst.* **122**, 349–361 (2018)
- Elliott, S.R.: A.c. conduction in amorphous chalcogenide and pnictide semiconductors. *Adv. Phys.* **36**(2), 135–217 (1987)
- El-Said Bakeer, D.: Elastic study and optical dispersion characterization of Fe-substituted cobalt aluminate nanoparticles. *Appl. Phys. A* **126**, 443 (2020)

- Fahim, A., Ghods, P., Burkan Isgor, O., Thomas, M.D.: A critical examination of corrosion rate measurement techniques applied to reinforcing steel in concrete. *Mater Corros.* **69**(12), 1784–1799 (2018)
- Giuntini, J.C., Zanchetta, J.V., Jullien, D., Eholie, R., Houenou, P.: Temperature dependence of dielectric losses in chalcogenide glasses. *J. Non-Cryst. Solids* **45**(1), 57–62 (1981)
- Han, J., Senos, A.M.R., Mantas, P.Q.: Deep donors in polycrystalline Mn-doped ZnO. *Mater. Chem. Phys.* **75**(1), 117–120 (2002)
- Huang, D., Zeng, X., Zheng, Y., Wang, X., Yang, Y.: Influence of process parameters on band gap of Al-doped ZnO film. *Front. Optoelectron.* **6**(1), 114–121 (2013)
- Irshad, K., Khan, M.T., Murtaza, A.: Synthesis and characterization of transition- metals-doped ZnO nanoparticles by sol-gel auto-combustion method. *Phys. B Condens. Matter* **543**, 1–6 (2018)
- Ismail, R.A., Ali, A.K., Ismail, M.M., Hassoon, K.I.: Preparation and characterization of colloidal ZnO nanoparticles using nanosecond laser ablation in water. *Appl. Nanosci* **1**, 45–49 (2011a)
- Ismail, R.A., Ali, A.K., Ismail, M.M., Hassoon, K.I.: Preparation and characterization of colloidal ZnO nanoparticles using nanosecond laser ablation in water. *Appl. Nanosci.* **1**, 45–49 (2011b)
- Jose, J., Khadar, A.: Role of grain boundaries on the electrical conductivity of nanophase zinc oxide. *Mater. Sci. Eng A* **304–306**, 810–813 (2001)
- Joshi, R., Kumar, P., Gaur, A., Asokan, K.: Structural, optical and ferroelectric properties of V doped ZnO. *Appl. Nanosci.* **4**, 531–536 (2014)
- Kamarulzaman, N., Kasim, M.F., Rusdi, R.: Band gap narrowing and widening of ZnO nanostructures and doped materials. *Nanoscale Res. Lett.* **10**, 346 (2015)
- Kant, R., Sharma, D., Bansal, A., Singh, R.: Structural, optical and dielectric properties of Al/Mn doped ZnO nanoparticles, a comparative study. *Mater. Technol.* **36**(9), 513–520 (2021)
- Khan, I., Khan, S., Nongjai, R., Ahmed, H., Khan, W.: Structural and optical properties of gel-combustion synthesized Zr doped ZnO nanoparticles. *Opt. Mater.* **35**, 1189–1193 (2013)
- Khan, R., Fashu, S., Rehman, Z.U.: Structural, dielectric and magnetic properties of (Al, Ni) co-doped ZnO nanoparticles. *J. Mater. Sci. Mater. Electron.* **28**(5), 4333–4339 (2017)
- Kumar, H., Rani, R.: Structural and optical characterization of ZnO nanoparticles synthesized by micro-emulsion route. *Int. Lett. Chem. Phys. Astron.* **19**, 26–36 (2013)
- Kumar, G.S., Raguram, T., Rajni, K.S.: Synthesis and characterization of Nickel-Substituted Cobalt Ferrite nanoparticles using Sol-Gel auto-combustion method. *J. Supercond. Nov. Magn.* **32**(6), 1715–1723 (2019)
- Li, X.D., Chen, T.P., Liu, Y., Leong, K.C.: Evolution of dielectric function of Al-doped ZnO thin films with thermal annealing: effect of band gap expansion and free-electron absorption. *Opt. Express* **22**(19), 23086–23093 (2014a)
- Li, X.D., Chen, T.P., Liu, P., Liu, Y., Leong, K.C.: A study on the evolution of dielectric function of ZnO thin films with decreasing film thickness. *J. Appl. Phys.* **115**(10), 103512 (2014b)
- Loane, R.F., Xu, P., Silcox, J.: Thermal vibrations in convergent-beam electron diffraction. *Acta Crystallogr. Sect. A Found. Crystallograph.* **47**(3), 267–278 (1991)
- Manikandan, A., Manikandan, E., Meenatchi, B., Vadivel, S., Jaganathan, S.K., Lachumananandasivam, R., Henini, M., Maaza, M., Aanand, J.S.: Rare earth element (REE) lanthanum doped zinc oxide (La:ZnO) nanomaterials: synthesis structural optical and antibacterial studies. *J. Alloy. Comp.* **723**, 1155–1161 (2017)
- Mazen, S.A., Zaki, H.M., Mansour, S.F.: Infrared absorption and dielectric properties of Mg-Zn ferrite. *Int. J. Pure Appl. Phys.* **3**(1), 40–48 (2007)
- Mehedi Hassan, M., Khan W., Azam, A., Naqvi, A.H.: Influence of Cr incorporation on structural, dielectric and optical properties of ZnO nanoparticles. *J. Ind. Eng. Chem.* **21**, 283–291 (2015)
- Mitra, P., Mondal, S.: Structural and morphological characterization of ZnO thin films synthesized by successive ion layer adsorption and reaction. *Prog. Theor. Appl. Phys.* **1**, 17–31 (2013)
- Modi, K.B., Raval, P.Y., Shah, S.J.: Raman and mossbauer spectroscopy and x-ray diffractometry studies on quenched copper-ferri-aluminates. *Inorg. Chem.* **54**(4), 1543–1555 (2015)
- Mohamed, W.S., Abu-Dief, A.M.: Synthesis, characterization and photocatalysis enhancement of Eu2O3-ZnO mixed oxide nanoparticles. *J. Phys. Chem. Solids* **116**, 375–385 (2018)
- Mohamed, W.S., Abu-Dief, A.M.: Impact of rare earth europium (RE-Eu3+) ions substitution on micro-structural, optical and magnetic properties of CoFe2-xEu3O4 nanosystems. *Ceram. Int.* **46**(10), 16196–16209 (2020)
- Mohamed, M., Sedky, A., Alshammari, A.S., Gandouzi, M.: Optical photoluminescence and ferromagnetic properties of Ni doped ZnO for optoelectronic applications. *J. Mater. Sci. Mater.* **32**, 5186–5198 (2021)

- Mohamed, W.S., Hadia, N.M.A., Bakheet, B.A., Alzaid, M., Abu-Dief, A.M.: Impact of Cu²⁺ cations substitution on structural, morphological, optical and magnetic properties of Co_{1-x}Cu_xFe₂O₄ nanoparticles synthesized by a facile hydrothermal approach. *Solid State Sci.* **125**, 10841 (2022)
- Mohamed, W.S., Alzaid, M., Abdelbaky, S.M., Amghouz, Z., García-Granda, S.: Impact of Co²⁺ substitution on microstructure and magnetic properties of Co_xZn_{1-x}Fe₂O₄ nanoparticles. *Nanomaterials* **9**, 1602 (2019)
- Morais, A., Torquato, R.A., Silva, U.C., Salvador, C., Chesman, C.: Effect of doping and sintering in structure and magnetic properties of the diluted magnetic semiconductor ZnO:Ni. *Cerâmica* **64**(372), 627–631 (2018)
- Muhammad, W., Ullah, N., Haroon, M., Abbasi, B.H.: Optical, morphological and biological analysis of zinc oxide nanoparticles (ZnO NPs) using *Papaver somniferum* L. *RSC Adv.* **9**, 29541–29548 (2019)
- Mukhtar, M., Munisa, L., Saleh, R.: Co-precipitation synthesis and characterization of nanocrystalline zinc oxide particles doped with Cu²⁺ ions. *Mater. Sci. Appl.* **3**(8), 543–551 (2012)
- Mustaqima, M., Liu, C.: ZnO-based nanostructures for diluted magnetic semiconductor. *Turk. J. Phys.* **38**, 429–441 (2014)
- Omri, K., Bettaibi, A., Khirouni, K., El Mir, L.: The optoelectronic properties and role of Cu concentration on the structural and electrical properties of Cu doped ZnO nanoparticles. *Phys. B Condens. Matter* **537**, 167–175 (2018)
- Othman, A.A., Othman, M.A., Ibrahim, E.M.M., Ali, M.A.: Sonochemically synthesized ZnO nanosheets and nanorods: annealing temperature effects on the structure, and optical properties. *Ceram. Int.* **43**, 527–533 (2017)
- Patange, S.M., Shirsath, S.E., Jadhav, S.P.: Elastic properties of nanocrystalline aluminum substituted nickel ferrites prepared by co-precipitation method. *J. Mol. Struct.* **1038**, 40–44 (2013)
- Raghu, P., Srinatha, N., Naveen, C.S., Mahesh, H.M., Angadi, B.: Investigation on the effect of Al concentration on the structural, optical and electrical properties of spin coated Al: ZnO thin films. *J. Alloys Compd.* **694**, 68–75 (2017)
- Ragupathi, C., Vijaya, J.J., Manikandan, A., Kennedy, L.J., Ragupathi, C., Vijaya, J.J., Manikandan, A., Kennedy, L.: Phytosynthesis of nanoscale ZnAl₂O₄ by using sesame (*Sesamum indicum* L) optical and catalytic properties. *J. Nanosci. Nanotechnol.* **13**(12), 8298–8306 (2013)
- Raja, K., Ramesh, P.S., Geetha, D.: Structural, FTIR and photoluminescence studies of Fe doped ZnO-nanopowder by co-precipitation method. *Spectrochim. Acta-A-Mol. Biomol. Spectrosc.* **131**, 183–188 (2014)
- Rajesh Babu, B., Tatarchuk, T.: Elastic properties and antistructural modeling for nickel-zinc ferrite-aluminates. *Mater. Chem. Phys.* **207**, 534–541 (2018)
- Ram, M., Bala, K., Sharma, H. and Negi, N.S.: Effect of Co doping on the structural and dielectric properties of ZnO nanoparticles. *AIP Conf.* 1731, 050104 (2016)
- Ramesh Babu, N.C., Valente, M.A., NarasimhaRao, N., Graça, M.P.F., Naga Raju, G., Piasecki, M., Kityk, I.V., Veeraiyah, N.: Low temperature dielectric dispersion and electrical conductivity studies on Fe₂O₃ mixed lithium yttrium silicate glasses. *J. Non-Cryst. Solids* **358**, 3175 (2012)
- Rao, T.P., Kumar, M.C.S., Safarullaha, A., Ganesan, V., Barman, S.R., Sanjeeviraja, C.: Physical properties of ZnO thin films deposited at various substrate temperatures using spray pyrolysis. *Physica B* **405**(9), 2226–2231 (2010)
- Rodnyi, P.A., Chernenko, K.A., Venevtsev, I.D.: Optika and spektroskopiya, mechanisms of ZnO luminescence in the visible spectral region. *Optics Spectros.* **125**(3), 357–363 (2018a)
- Rodnyi, P.A., Chernenko, K.A., Venevtsev, I.D.: Mechanisms of ZnO luminescence in the visible spectral region. *Optika Spektroskopiya* **125**(3), 357–363 (2018b)
- Rusu, D.I., Rusu, G.G., Luca, D.: Structural characteristics and optical properties of thermally oxidized zinc films. *Acta Phys. Pol., A* **119**(6), 850–856 (2011)
- Saadi, H., Rhouma, F.I.H., Benzarti, Z., Bougrioua, Z., Guermazi, S., Khirouni, K.: Electrical conductivity improvement of Fe doped ZnO nanopowders. *Mater. Res. Bull.* **129**, 110884 (2020)
- Sagadevan, S., Pal, K., Chowdhury, Z.Z., Hoque, M.E.: Structural, dielectric and optical investigation of chemically synthesized Ag-doped ZnO nanoparticles composites. *J. Sol-Gel Sci. Technol.* **83**(2), 394–404 (2017)
- Sajid Ali, A., Ambreen, N., Bushara, F., Khan, W., Naqvi, A.H.: Investigation on structural, optical and dielectric properties of Co doped ZnO nanoparticles synthesized by gel-combustion route. *Mater. Sci. Eng. B* **177**, 428–435 (2012)
- Samanta, A., Goswami, M.N., Mahapatra, P.K.: Magnetic and electric properties of Ni-doped ZnO nanoparticles exhibit diluted magnetic semiconductor in nature. *J. Alloys Compd.* **730**, 399–407 (2018)

- Samanta, A., Goswami, M.N., Mahapatra, P.K.: Fe-doped ZnO nanoparticles as novel photonic and multiferroic semiconductor. *Mater. Chem. Phys.* **240**, 122180 (2020)
- Santhoshkumar, J., Kumar, S.V., Rajeshkumar, S.: Synthesis of zinc oxide nanoparticles using plant leaf extract against urinary tract infection pathogen. *Resour. Effic. Technol.* **3**(4), 459 (2017)
- Sedky, A., Abu-Abdeen, M., Almulhem, A.A.A.: Nonlinear I-V characteristics in doped ZnO based-ceramic varistor. *Physica B* **388**, 266–273 (2007)
- Sedky, A., Youssif, M.I., El-Brollosy, T.A.: Photoacoustic and Ac impedance measurements of ZnO varistors with ZnO nanoparticles addition. *Nat. Sci.* **14**(2), 66–73 (2016)
- Sedky, A., Amin, S.A., Mohamed, M.: Electrical, photoluminescence and ferromagnetic characterization of pure and doped ZnO nanostructures. *Appl. Phys. A* **125**, 308 (2019)
- Sedky, A., Ali, A.M., Mohamed, M.: Structural and optical investigation of pure and Al doped ZnO annealed at different temperatures. *Opt. Quantum Electron.* **52**(42), 1–12 (2020)
- Sedky, A., Ali, A.M., Mansour, M.: Electrical, photoluminescence and optical investigation of ZnO nanoparticles sintered at different temperatures. *Opt. Quantum Electron.* **52**(42), 1–21 (2020)
- Sedky, A., Ali, A.M., Al Grani, H.: Structural, FTIR, optical and magnetic investigation of Zn1-xMxO ceramics with M= Cu, Mn: comparative study. *J. Alloys Compd.* **912**, 165139 (2022a)
- Sedky, A., Afify, N., Ali, A.M., Algarni, H.: On the dielectric behaviors of Zn1-x-yFexMyO ceramics for nonlinear optical and solar cell devices. *Appl. Phys. A*, **128**, 2 (2022b)
- Seetawan, U., Jugsujinda, S., Seetawan, T., Ratchasin, A., Euvananont, C., Junin, C., Thanachayanont, C., Chainaronk, P.: Effect of calcinations temperature on crystallography and nanoparticles in ZnO disk. *Mater. Sci. Appl.* **2**(9), 1302 (2011)
- Selvakumar, S., Murugaraj, R., Viswanathan, E., Sankar, S., Sivaji, K.: Dielectric properties and relaxation mechanism of organic trans-stilbene and p-terphenyl molecular crystals using impedance spectroscopy. *J. Mol. Struct.* **1056–1057**, 152–156 (2014)
- Shahedi, Z., Jafari, M.R.: Synthesis Al complex and investigating effect of doped ZnO nanoparticles in the electrical and optical efficiency of OLEDs. *Appl. Phys. A* **123**, 98 (2017)
- Singh, J., Singh, R.C.: Structural, optical, dielectric and transport properties of ball mill synthesized ZnO-V₂O₅ nano-composites. *J. Mol. Struct.* **1215**, 128261 (2020)
- Singh, J., Singh, R.C.: *J. Mol. Struct.* **1215**, 128261 (2020b)
- Singh, S., Dey, P., Roy, J.N., Mandal, S.K.: Tunable dielectric constant with transition metal doping in Zn1-x(MnTM)xO (TM 1/4 Co, Fe) nanocrystals. *J. Alloys Compd.* **642**, 15–21 (2015)
- Singh, J., Singh, R.C.: Enhancement of optical, dielectric and transport properties of (Sm, V) co-doped ZnO system and structure-property correlations. *Ceram. Int.* **47**, 10611–10627 (2021)
- Singh, J., Virpal, Sharma, S., Singh, R.C.: Effect of Fe₂O₃ doping on structural properties of ZnO-V₂O₅ based varistor system. *AIP Conference Proc.* **1832**, 120021 (2017)
- Srinivasan, N., Kannan, J.C.: Investigation on room temperature photoluminescence of pure and aluminum doped zinc oxide nanoparticles. *Mater. Sci. Poland* **33**, 205–212 (2015)
- Srinivasulu, T., Saritha, K., Ramakrishna Reddy, K.T.: Synthesis and characterization of Fe-doped ZnO thin films deposited by chemical spray pyrolysis. *Modern Electron. Mater.* **3**(2), 76–85 (2017)
- Tong, H., Deng, Z., Liu, Z., Huang, C., Huang, J., Lan, H., Wang, C., Cao, Y.: Effects of post-annealing on structural, optical and electrical properties of Al-doped ZnO thin films. *Appl. Surf. Sci.* **257**(11), 4906–4911 (2011)
- Tripathi, R., Kumar, A., Bharti, C., Sinha, T.P.: Dielectric relaxation of ZnO nanostructures synthesized by soft chemical method. *Curr. Appl. Phys.* **10**, 676–681 (2010)
- Vempati, S., Mitra, J., Dawson, P.: One-step synthesis of ZnO nanosheets: a blue-white fluorophore. *Nanoscale Res. Lett.* **7**, 470 (2012)
- Wan-Abdullah, W.R., Zakaria, A., Ghazali, M.S.: Synthesis mechanism of low-voltage praseodymium oxide doped zinc oxide varistor ceramics prepared through modified citrate gel coating. *Int. J. Mol. Sci.* **13**(4), 5278–5289 (2012)
- Wang, X., Zhang, Y.: The effects of UV radiation on the structure and properties of AZO thin films deposited on quartz glass by magnetron sputtering. *Mater. Lett.* **188**, 257–259 (2017)
- Wasly, H.S.: X-ray analysis for determination the crystallite size and lattice strain in zno nanoparticles. *J. Al Azhar Univ. Eng. Sector* **13**(49), 1312 (2018)
- Wojnarowicz, J., Chudoba, T., Koltsov, I., Gierlotka, S., Dworakowska, S., Lojkowski, W.: Size control mechanism of ZnO nanoparticles obtained in microwave solvothermal synthesis. *Nanotechnology* **29**(6), 065601 (2018)
- Yang, Z.: A perspective of recent progress in ZnO diluted magnetic semiconductors. *Appl. Phys. A* **112**, 241–254 (2013)
- Zamiri, R., Kaushal, A., Rebelo, A., Ferreira, J.M.F.: Er doped ZnO nanoplates: synthesis, optical and dielectric properties. *Ceram. Int.* **40**, 1635–1639 (2013)

- Zamiri, R., Singh, B., Belsley, M.S., Ferreira, J.M.: Structural and dielectric properties of Al-doped ZnO nanostructures. *Ceram. Int.* **40**(4), 6031–6036 (2014)
- Zamiri, R., Kaushal, A., Rebelo, A., Ferreira, J.M.F.: Er doped ZnO nanoplates: synthesis, optical and dielectric properties. *Ceram Int.* **40**, 1635–1639 (2014a)
- Zamiri, R., Singh, B., Bdkin, I., Rebelo, A., Belsley, M.S., Ferreira, J.M.F.: Influence of Mg doping on dielectric and optical properties of ZnO nano-plates prepared by wet chemical method. *Solid State Commun.* **195**, 74–79 (2014b)
- Zeyada, H.M., El-Taweel, F.M., El-Nahass, M.M., ElShabaan, M.M.: Effect of substitution group on dielectric properties of 4H-pyrano [3, 2-c] quinoline derivatives thin films. *Chin. Phys. B* **25**(7), 077701 (2016)
- Zhai, C.H, Zhang, R.J, Chen, X., Zheng, Y.X., Wang, S.Y., Liu, J., Dai, N., Chen, L.Y.: Effects of Al doping on the properties of ZnO thin films deposited by atomic layer deposition. *Nanoscale Res. Lett.* **11**(1), 407–414
- Zhao, X., Xia, C., Wang, T., Dai, X.: Electronic and magnetic properties of X-doped (X = Ti, Zr, Hf) tungsten disulphide monolayer. *J. Alloys Compd.* **654**, 574–579 (2016)
- Zhou, Z., Sato, N., Komaki, T., Koizumi, A., Komori, T., Morinaga, M., Fujiwara, Y., Takeda, Y.: Effects of S-doping and subsequent annealing on photoluminescence around 154 μm from Er-containing ZnO. *Mater. Sci. Forum* **475–479**, 1125–1128 (2005)

Publisher's Note Springer Nature remains neutral with regard to jurisdictional claims in published maps and institutional affiliations.